Nonparametric Methodology to Estimate Precipitating Ice from Multiple-Frequency Radar Reflectivity Observations

MIRCEA GRECU AND LIN TIAN[a]

Goddard Earth Sciences Technology and Research, Morgan State University, Baltimore, and Laboratory for Atmospheres, NASA Goddard Space Flight Center, Greenbelt, Maryland

GERALD M. HEYMSFIELD

Laboratory for Atmospheres, NASA Goddard Space Flight Center, Greenbelt, Maryland

ALI TOKAY AND WILLIAM S. OLSON

Joint Center for Earth Systems Technology, University of Maryland, Baltimore County, Baltimore, and Laboratory for Atmospheres, NASA Goddard Space Flight Center, Greenbelt, Maryland

ANDREW J. HEYMSFIELD AND AARON BANSEMER

National Center for Atmospheric Research,[b] Boulder, Colorado

(Manuscript received 5 February 2018, in final form 18 September 2018)

ABSTRACT

In this study, a nonparametric method to estimate precipitating ice from multiple-frequency radar observations is investigated. The method does not require any assumptions regarding the distribution of ice particle sizes and relies on an efficient search procedure to incorporate information from observed particle size distributions (PSDs) in the estimation process. Similar to other approaches rooted in optimal-estimation theory, the nonparametric method is robust in the presence of noise in observations and uncertainties in the forward models. Over 200 000 PSDs derived from in situ observations collected during the Olympic Mountains Experiment (OLYMPEX) and Integrated Precipitation and Hydrology Experiment (IPHEX) field campaigns are used in the development and evaluation of the nonparametric estimation method. These PSDs are used to create a database of ice-related variables and associated computed radar reflectivity factors at the Ku, Ka, and W bands. The computed reflectivity factors are used to derive precipitating ice estimates and investigate the associated errors and uncertainties. The method is applied to triple-frequency radar observations collected during OLYMPEX and IPHEX. Direct comparisons of estimated ice variables with estimates from in situ instruments show results consistent with the error analysis. Global application of the method requires an extension of the supporting PSD database, which can be achieved through the processing of information from additional past and future field campaigns.

1. Introduction

Estimates of precipitation derived from single-frequency radar observations are inherently uncertain. This is because to express accurately the distribution of the number of precipitation particles in an observation volume as a function of their sizes more than one variable is necessary, whereas single-frequency radars provide only one reflectivity observation per volume. Solid precipitation is characterized by an additional type of significant uncertainty stemming from the fact that electromagnetic-scattering properties of solid precipitation cannot be uniquely expressed as a function of their equivalent sizes (defined as the size of an equivalent spherical raindrop resulting from melting the solid precipitation) (Kuo et al. 2016). Collocated dual- and triple-frequency radar observations may be effectively used to mitigate these uncertainties because reflectivity

Denotes content that is immediately available upon publication as open access.

[a] Deceased.

[b] The National Center for Atmospheric Research is sponsored by the National Science Foundation.

Corresponding author: Mircea Grecu, mircea.grecu-1@nasa.gov

DOI: 10.1175/JAMC-D-18-0036.1

observations at additional frequencies may be used to estimate explicitly an additional parameter.

In this study, we investigate the estimation of precipitation above the freezing level in both winter and summer storms from airborne collocated triple-frequency radar observations. The frequencies of the radar observations are 13.91 GHz (Ku band), 35.56 GHz (Ka band), and 94.0 GHz (W band). Previous studies showed that different ice particles have different signatures in dual-wavelength-reflectivity-ratio (DWR) space (Kneifel et al. 2011). To be specific, when triple-frequency radar observations are available, two independent DWRs, where the DWR for two frequencies λ_1 and λ_2 is defined as

$$\mathrm{DWR}_{\lambda_1,\lambda_2} = 10\log\left[\frac{Z(\lambda_1)}{Z(\lambda_2)}\right],$$

can be defined. Kneifel et al. (2011) showed that different particle shapes have different signatures in the $\mathrm{DWR_{KuKa}}$–$\mathrm{DWR_{KaW}}$ plane. Subsequent observational and modeling studies (Kulie et al. 2014; Kneifel et al. 2015; Leinonen and Szyrmer 2015) demonstrated that the triple-frequency signatures predicted by the theoretical calculations have practical relevance and may be linked to cloud microphysical processes such as riming and aggregation. Although not every single ($\mathrm{DWR_{KuKa}}$, $\mathrm{DWR_{KaW}}$) combination can be uniquely associated with an ice particle type, it is expected that the use of triple-frequency radar observations facilitates the derivation of more accurate estimates of bulk properties (e.g., equivalent water content and mass mean diameter) of precipitating ice.

The method used in this study to estimate ice from triple-frequency radar observations is based on a large dataset of ice particle size distributions (PSDs) derived from in situ observations collected during field campaigns and an ensemble Kalman smoother (EnKS; Evensen 2006) embedded into a forward attenuation correction procedure. The PSDs are used to calculate triple-frequency radar reflectivity factors that are used by a statistical procedure to inversely relate reflectivity observations to PSDs. The electromagnetic-scattering properties of ice particles are derived from publicly available scattering databases (Liu 2008; Lu et al. 2016). Details are provided in section 2 below. A particular property of the EnKS that may be used to derive efficient and accurate estimates from multiple-instrument observations is that the observations can be processed sequentially (Evensen 2006). This property can be exploited to limit the number of calculations needed to derive the estimates by processing the observations characterized by low computational cost (e.g., radar observations not affected by multiple scattering) first and then narrowing down the range of possible solutions before processing observations characterized by high computational costs (e.g., radar observations affected by multiple scattering). Moreover, because triple-frequency reflectivity values are calculated for every PSD in the large dataset, a cross-validation approach may be devised to characterize the uncertainties of the ice estimates. Specifically, the PSD and associated database can be randomly split into two subsets. The first subset is used to provide the information needed by the estimation procedure, and the second is used for evaluation. That is, the reflectivity factors in the second dataset are used to derive multiple-frequency radar estimates of ice properties. These estimates are compared with the reference values (derived directly from the PSDs in the second dataset), and various statistical scores (correlation coefficient, relative bias, etc.) may be derived. We employ this strategy to characterize the performance of the nonparametric strategy in section 3.

Similar to more traditional approaches that are based on optimal-estimation theory (e.g., Delanoë and Hogan 2008; Grecu et al. 2011; Battaglia et al. 2016), the nonparametric method is robust in the presence of noise in the observations and uncertainties in the underlying forward models. However, unlike those approaches, this method does not require explicit assumptions on the PSD used in the forward models and does not require an explicit description of the "a priori" joint distributions of PSD properties. The global application of the nonparametric method requires global PSD information, but this is a requirement for the optimal-estimation-theory approaches of Delanoë and Hogan (2008), Grecu et al. (2011), and Battaglia et al. (2016) as well.

In section 4, the estimation method formulated in the study is applied to triple-frequency radar observations collected during the Olympic Mountains Experiment (OLYMPEX; Houze et al. 2017) and the Integrated Precipitation and Hydrology Experiment (IPHEX; Barros et al. 2014). Results are consistent with those derived in the cross-validation analysis and are in good agreement with collocated in situ measurements. A summary and conclusions are provided in the last section of the paper.

2. Method

a. Particle size distributions

An essential concept in relating various microphysical properties of falling ice particles to radar observations is the PSD (Sekhon and Srivastava 1970). In mathematical terms, the PSD is the derivative of the concentration of ice particles smaller than a size with respect to that size (Sekhon and Srivastava 1970). Although the gamma

function was found to represent well the variability of observed PSDs (Heymsfield et al. 2002, 2018), in this study we do not use analytical functions to relate PSDs to observed reflectivities. Instead, we use directly observed PSDs to calculate the associated reflectivities at the Ku, Ka, and W bands using accurate electromagnetic-scattering models and use an efficient database-navigation procedure to inversely relate observed radar reflectivities to PSDs. The PSDs are derived from measurements by a two-dimensional stereo probe (2D-S; Lawson et al. 2006) and two orthogonally mounted High Volume Precipitation Spectrometers (HVPS-3) on board the University of North Dakota (UND) Cessna Citation airplane during OLYMPEX (Houze et al. 2017) and IPHEX (Barros et al. 2014) using the method of Heymsfield et al. (2018). The particle number concentration normalized by bin width is specified for 41 particle size bins. The bin centers vary from 50 μm to 2.75 cm. The number concentrations for particles larger than 1.0 mm are specified from HVPS-3 observations, while the number concentrations from particles smaller than 1.0 mm are derived from 2D-S observations.

The diameter of the minimum enclosing circle is used to define the size of an ice particle (Wu and McFarquhar 2016). It should be mentioned that the size of the observed particles can be underestimated if the particle's maximum dimension is not oriented with the imaging plane, or if the image extends beyond the edge of the picture. Particle size can also be overestimated if a particle is poorly focused, breaking apart, or if there are coincident particles in the sample area. Despite these limitations, the PSDs derived from in situ observations are extremely valuable in the development and evaluation of methodologies to estimate ice properties from radar observations.

The PSD data used in this study are available from the OLYMPEX and IPHEX data portals. The PSD data are integrated to derive the associated equivalent reflectivity factors at Ku, Ka, and W band. This procedure is described next.

b. Radar backscattering

The main challenge in quantifying the electromagnetic-scattering properties of realistic snowflakes and ice particles at microwave frequencies is that they exhibit complex shapes that make the numerical solutions to Maxwell's equations so computationally expensive that they were almost intractable until a few years ago. Nevertheless, several publicly available ice-scattering databases have been developed over the years (Liu 2008; Lu et al. 2016; Kuo et al. 2016). In this study, we use the Liu (2008) and Lu et al. (2016) databases. The equivalent radar reflectivity factor is derived as

$$Z = \frac{\lambda^4}{|K_w|^2 \pi^5} \sum_{i=1}^{41} \sigma_b(D_i) N(D_i), \tag{1}$$

where λ is the wavelength, K_w is the dielectric factor of water, $\sigma_b(D_i)$ is the average backscatter cross section for size bin number i, and $N(D_i)$ is the associated concentration of particles.

Given that the backscatter cross section of an ice particle is much more strongly related to its mass than to its maximum diameter (Kuo et al. 2016), the backscatter variable in Eq. (1) is expressed as a function of the associated mass $m_i(D_i)$ rather than the associated D_i. Heymsfield et al. (2010) showed that although the relationships between the mass and the maximum dimension of a snowflake can vary significantly as a function of the type of the cloud in which the snowflake is observed, a mass–dimensional relationship of the type $m = aD^b$ with $a \approx 0.0061$ and $b \approx 2.05$ (in cgs units) works well in a broad range of conditions in midlatitude storms. Therefore, the relationship $m = 0.0061D^{2.05}$ is used to convert the PSD size bins in Eq. (1) to equivalent mass bins. The ice particles from the scattering databases of Liu (2008) and Lu et al. (2016) are assigned to the PSD mass bins and the average backscatter and extinction cross sections as well as the associated mass are calculated for every bin. Then, an interpolation procedure is applied to determine the backscatter and extinction cross sections corresponding to the mass bin centers. The interpolation functions are second-order polynomials that relate the logarithm of the particle mass to the logarithm of the backscatter and extinction sections.

Shown in Fig. 1 are the backscatter and extinction sections as a function of the particle mass for three types of particles: Liu (2008) aggregates, Lu et al. (2016) aggregates, and Lu et al. (2016) graupel. For the brevity of notation, Liu (2008) particles are marked as ScatDB in Fig. 1, and Lu et al. (2016) particles are marked as PSU. The impact of the assumed particle on estimates is studied in section 3, but meanwhile it is useful to note that the backscatter and extinction sections tend to depend on the particle type. As expected, the graupel particles are characterized by larger backscatter sections than the other two (less dense) types of particles. Also, the Liu (2008) aggregates, which tend to be slightly denser than Heymsfield et al. (2010) aggregates (i.e., $m = 0.0061D^{2.05}$), generally exhibit larger backscattering than the Lu et al. (2016) aggregates. This is not surprising given that Lu et al. (2016) aggregates tend to be significantly less dense than those of Heymsfield et al. (2010). It is interesting to note that the Rayleigh–Gans-based theory

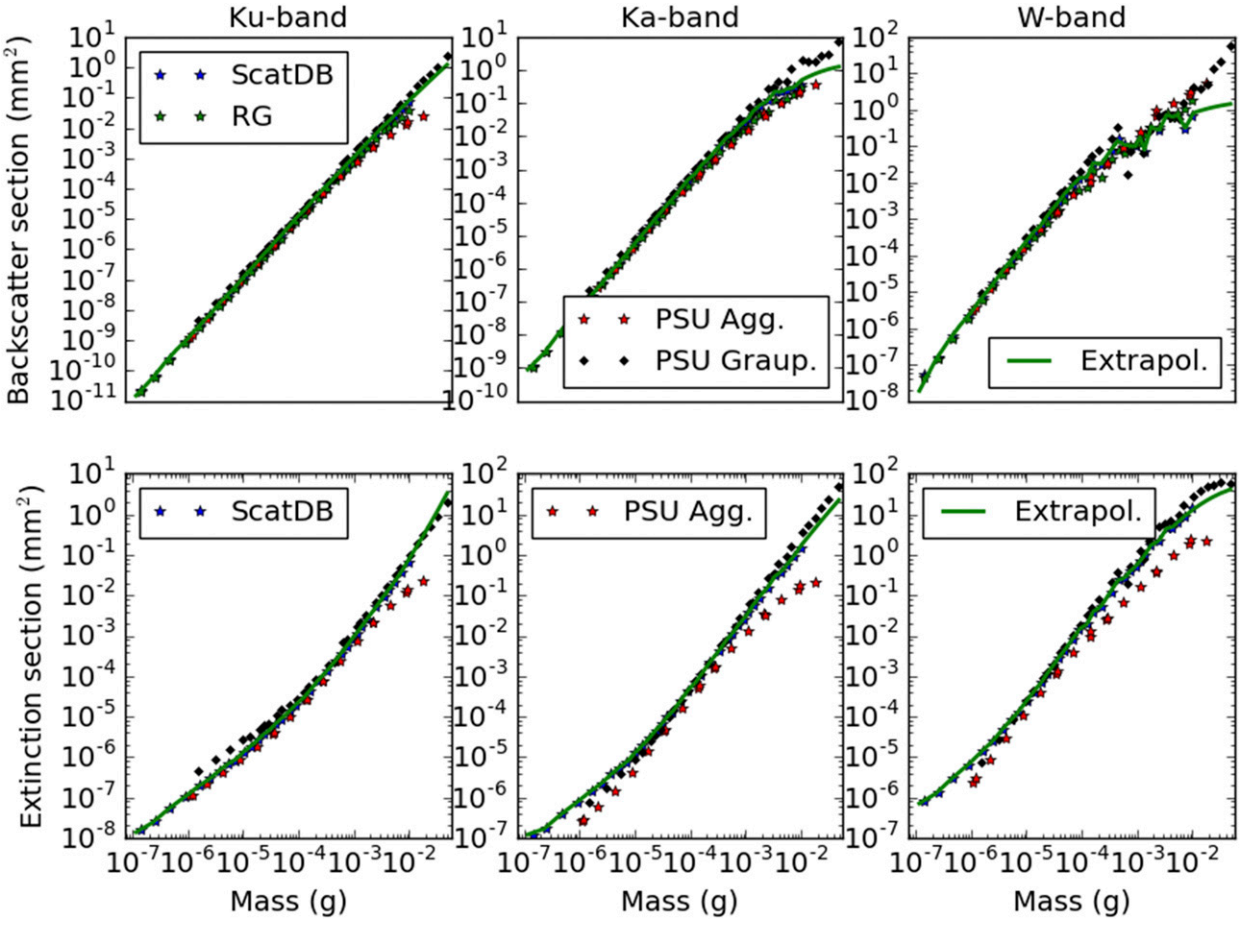

FIG. 1. Averaged ice particle (top) backscatter cross sections and (bottom) extinction cross sections at (left) Ku, (center) Ka, and (right) W bands, plotted as functions of the particle mass. Results from four types of particles are shown: 1) Liu (2008), symbolized by blue stars and labeled as ScatDb; 2) Lu et al. (2016) aggregates, symbolized by red stars and labeled as PSU Agg.; 3) Lu et al. (2016) graupel, symbolized by blue diamonds and labeled as PSU Graup.; and 4) Westbrook et al. (2006) (green stars labeled as RG) particles whose backscatter properties were derived using the formula derived by Westbrook et al. (2008) from Rayleigh–Gans calculations. The green lines represent the fitted analytical formulas to the Liu (2008) particles.

of Westbrook et al. (2006, 2008) provides reasonable backscatter estimates, that is, close to the backscatter sections of Liu (2008) and between the Lu et al. (2016) graupel and Lu et al. (2016) aggregates backscatter sections. Also, note that the polynomial functions fit almost perfectly the existing backscatter and extinction data and provide a reasonable extrapolation for the mass bins for which calculations do not exist (i.e., particles with a liquid-equivalent-mass diameter that is larger than 3.5 mm).

Results shown in Fig. 1 are derived while assuming random orientation of particles. Recent work that is based on the analysis of observations from the Global Precipitation Measurement Microwave Imager suggests that significant particle orientation occurs near convective outflow regions (Gong and Wu 2017). Although from the radar remote sensing perspective, particle orientation is important, there is too little particle-orientation-related information in the observations considered in this study to reliably quantify or account for it.

Once the backscatter and extinction properties are determined for each size bin, the integration of PSDs to determine the associated reflectivity at Ku, Ka, and W bands is straightforward. However, the inverse operation (i.e., determining various PSD descriptors from a triplet of Ku-, Ka-, and W-band reflectivity observations) is not straightforward because the same reflectivity triplet can be reproduced by multiple PSDs. Delanoe et al. (2014) showed that normalizing the reflectivity factors and the ice water contents (IWC, defined as the mass integral over the entire PSD) by a scale factor N_w significantly reduces the spread in reflectivity versus IWC relationships. It follows that any collection

of PSDs that exhibits large variability in N_w is characterized by ambiguities in the associated reflectivity factors. The scale factor N_w is proportional to the ratio of the IWC to the fourth power of the mean mass diameter D_m and may be readily derived from the PSD data (Delanoe et al. 2014).

Shown in Fig. 2 are contoured frequency-by-altitude displays (CFADs) of the logarithm of the scale factor and of the mass mean diameter derived using all PSD data collected during OLYMPEX. The method to derive the PSD parameters from the cloud probes is described in Heymsfield et al. (2004). As is apparent in Fig. 2, there is significant variability in the distribution of N_w. Also, the scaling factor tends to increase with height, while the mass mean diameter generally decreases with height. This is consistent with the findings of Delanoe et al. (2014). In this study, unlike in the approach of Grecu et al. (2011), we do not attempt to explicitly estimate N_w and use N_w-dependent parameterized relationships to estimate the ice water content and the mass mean diameter from reflectivity observations, but instead use a nonparametric approach akin to ensemble Kalman smoothing. This is explained next.

c. *Nonparametric estimation*

To mitigate ambiguities in the observations, geophysical estimation algorithms traditionally rely on two strategies. One is the use of databases of state variables and associated observations, as well as statistical methods, to relate the observations to the state variables. The other is the use of forward physical models between state variables and their associated observations and optimization methods that maximize the agreement between the forward models and observations while penalizing discrepancies between the estimates and their climatology. Our approach falls within the first category. A widely used formulation in this category is the Goddard profiling algorithm (GPROF; Kummerow et al. 2015). Unlike GPROF, our method uses a procedure that is formally identical to the EnKS (Evensen 2006) to derive estimates that are based on the agreement between actual observations and the observations in the database.

In specific terms, an efficient range search (Agarwal and Erickson 1999) is carried out to find all of the entries in the PSD database characterized by triple-frequency observations within 1.5 dB from the actual observations. The range search is implemented using hierarchical data structures called ''ball-trees'' (Liu et al. 2006). The efficiency of the range search stems from the fact that only subtrees that intersect the 1.5-dB sphere centered on the observations need to be explored. Whether the intersection of a subtree with the 1.5-dB sphere results in a nonvoid set may be readily determined without actually evaluating the distances between all of the points in the subtree and the ball spheres (Liu et al. 2006). If the range search returns fewer than 50 records in the database, we relax the search condition to determine the 50 records closest to the observations. The number 50 was established using a sensitivity analysis. Specifically, we considered 1000 records and found that while estimates are not significantly different, the computational time increased by almost a factor of 2.0. Once the database records within 1.5 dB of the observations (or the 50 records closest to the observations) are determined, an EnKS is applied to derive estimates of various PSD-related variables (mass, mass mean diameter, calculated specific attenuation, etc.). That is, given the set of PSD-related variables $\mathbf{x}$ and associated observations $\mathbf{y}$ produced by the search, one can use a simple linear regression to investigate the relationship between perturbations in $\mathbf{y}$ and $\mathbf{x}$ (Anderson 2003). Mathematically, perturbations $\delta\mathbf{x}$ and $\delta\mathbf{y}$ are related through

$$\delta\mathbf{x} = \mathrm{Cov}(\mathbf{x},\mathbf{y})\mathrm{Cov}(\mathbf{y},\mathbf{y})^{-1}\delta\mathbf{y}\,, \tag{2}$$

where $\mathrm{Cov}(\mathbf{x},\mathbf{y})$ is the covariance of $\mathbf{x}$ with $\mathbf{y}$ and $\mathrm{Cov}(\mathbf{y},\mathbf{y})$ is the covariance of $\mathbf{y}$ with itself. The $\delta\mathbf{x}$ adjustment that makes $\mathbf{y}$ equal to the actual observations is

$$\delta\mathbf{x}_{\mathrm{adj}} = \mathrm{Cov}(\mathbf{x},\mathbf{y})\mathrm{Cov}(\mathbf{y},\mathbf{y})^{-1}(\mathbf{y}_{\mathrm{obs}} - \overline{\mathbf{y}}), \tag{3}$$

where $\mathbf{y}_{\mathrm{obs}}$ is the observation vector and $\overline{y}$ is the average of $\mathbf{y}$. Note that Eq. (3) is formally identical to the EnKS update (Evensen 2006) if the observation and modeling uncertainties are included in $\mathbf{y}$. This is the reason why the computed reflectivities in the database are perturbed through the addition of random noise with mean 0.0 and standard deviation 1.0 dB. It should be mentioned that the magnitude of uncertainties in the computed reflectivities may be larger than considered here. However, with an exception, instead of increasing the standard deviation of the perturbed observations, in the next section, we explicitly investigate the impact of uncertainties in the computed reflectivities by assuming one type of particle in the database creation and deriving estimates from reflectivities computed using a potentially different type of particles. In addition, we also investigate the impact of supercooled cloud water on attenuation correction.

Given that EnKSs are Bayesian estimation methods, and Eq. (2) is an EnKS that is based on a particular type of localization (Petrie and Dance 2010), the nonparameteric estimation method formulated in this study, henceforth referred to as nPEnKS, is a quasi-Bayesian method. The database of PSDs and associated reflectivity used in nPEnKS will be referred to as the

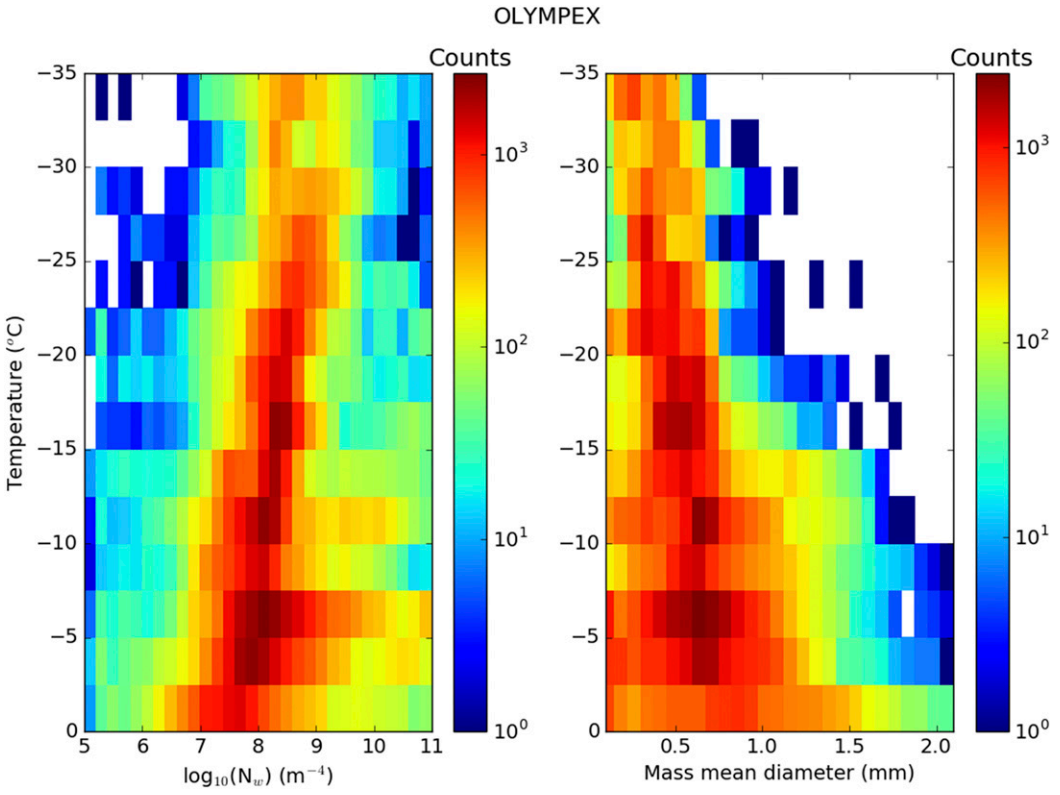

FIG. 2. (left) CFADs of (left) the logarithm of the scale factor N_w and (right) D_m for PSD derived from OLYMPEX in situ observations.

a priori database although its use is not the same as in a fully Bayesian estimation algorithm (Kummerow et al. 2015). At the most fundamental level, however, no significant differences between the two approaches are expected. Nevertheless, nPEnKS is expected to be more flexible when applied to complex observations. This is because, as mentioned before, the observations can be processed sequentially (Evensen 2006), which allows for the derivation of preliminary estimates on the basis of partial observations (e.g., Ku- and Ka-band observations) and the computation of more complex observations (W-band observations affected by multiple scattering, radiometer observations, etc.) on the fly and their inclusion in the derivation of the final estimates. We mention that the application of the multiple-scattering radar model of Hogan and Battaglia (2008) does not suggest significant multiple scattering in the observations used in this study, but for the application of nPEnKS to satellite observations the inclusion of a multiple-scattering model in the framework is necessary (Grecu et al. 2016).

Note that because the simulated reflectivities in the database are not affected by attenuation, reflectivity observations $\mathbf{y}_{\text{obs}}$ are corrected for attenuation before being used in Eq. (3). In our implementation, this is achieved through a gate-by-gate attenuation correction procedure. The attenuation correction accounts for attenuation due to ice particles, water vapor, and cloud water. The attenuation by water vapor and cloud water is explained in section 4. The attenuation due to ice particles involves an iterative process. As previously mentioned, the attenuation associated with the observed PSDs in the database is calculated and saved in the augmented PSD scattering database. This allows for the calculation of two-way integrated attenuation from the top of the atmosphere to the center of the radar gate being processed. The two-way integrated attenuation is added to the reflectivity observations, and IWC, D_m, and the attenuation at all frequencies are iteratively derived. The attenuation from the upper boundary of the current gate to its center is initially assumed to be zero, and IWC, D_m, and the attenuation are derived. In the next iteration, potentially different IWC, D_m, and attenuation estimates are derived because new estimates of the attenuation within the radar gate are available. The process is repeated until convergence is achieved. This type of attenuation correction may become unstable if carried out through the melting layer, but it works properly if it is limited to the ice phase only.

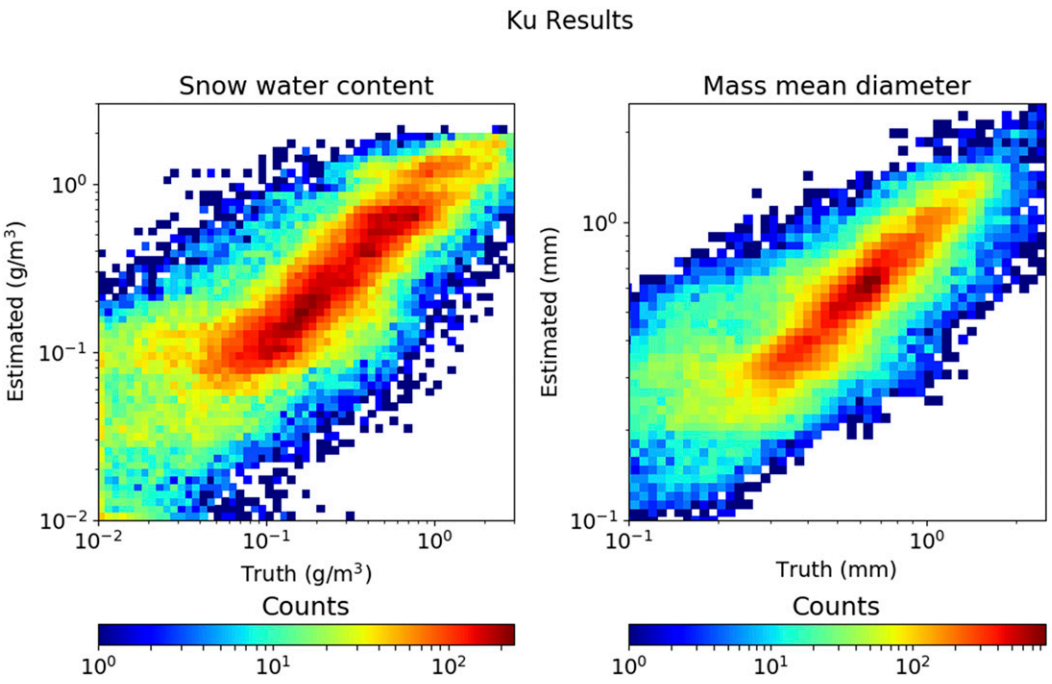

FIG. 3. Estimated (left) IWC and (right) D_m derived from computed Ku-band reflectivity observations vs the respective true IWC and D_m used in the observations synthesis. The PSD data used in the computation of the reflectivities are derived from aircraft observations in OLYMPEX.

To predict the particle type using the range search method, for each PSD derived from in situ observations we compute three sets of associated Ku-, Ka-, and W-band reflectivity (i.e., one set per particle type). A particle-type identifier is included in the merged PSD reflectivity dataset, and when the range searches are performed each PSD within the search domain is associated with a particle type. The most likely particle type is determined through weighted majority voting (Hastie et al. 2009), where the weights are determined as the probability of the differences between the observed and computed reflectivities, assuming that these differences are governed by a multivariate normal distribution with mean 0.0 and standard deviation 1.0 dB.

3. Uncertainty analysis

The explicit existence of a database of PSD and associated reflectivity factors makes it straightforward to investigate the uncertainty associated with our multiple-frequency estimation method. This is because, as previously mentioned, the database may be randomly separated into two disjoint subsets and used for cross-validation evaluation. That is, one set is used to provide the a priori (background) information [i.e., $\mathbf{x}$ and $\mathbf{y}$ in Eq. (3)] while the other set is used to provide the observations $\mathbf{y}_{\text{obs}}$ and the true PSD parameters associated with these observations.

As is apparent in Fig. 2, the N_w distribution strongly depends on the temperature. We therefore include the temperature as a parameter in the range search meant to find the records in the PSD-reflectivity database similar to the reflectivity observations in the evaluation database. Frequency contour plots of IWC and D_m estimated from Ku-only reflectivity observations relative to their true distributions are shown in Fig. 3. Results in Fig. 3 are derived using PSD data from OLYMPEX and assuming that all particles are Liu (2008) aggregates. Despite significant scatter, there is good agreement between the estimates and the reference variables even when Ku-only reflectivity observations are used in the estimation. The scatter decreases and the agreement improves when the Ka- and the Ka- and W-band reflectivity observations are used in the estimation. This is shown in Figs. 4 and 5. Three performance parameters—that is, the cross-correlation coefficient (CC), the normalized root-mean-square error (NRMSE), and the normalized mean error (NME) (Wilks 2011)—that describe the agreement between estimated IWC and D_m and their true values are reported in Table 1. As is apparent in Table 1 and consistent with Fig. 3, there is little improvement with the inclusion of the Ka-band observations in the estimation method, although there is

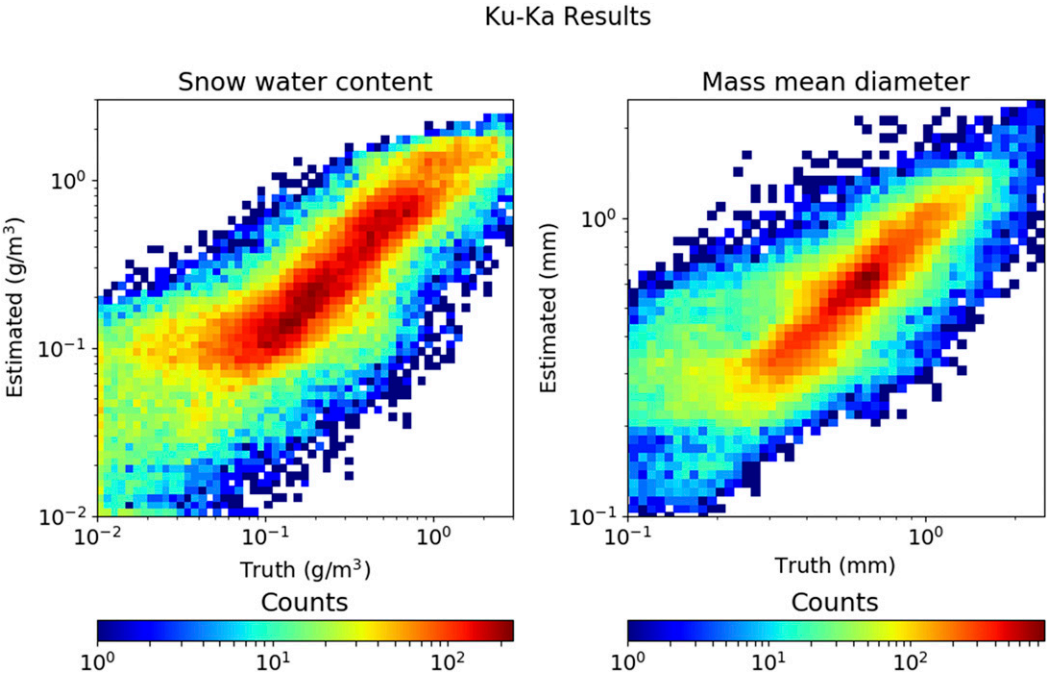

FIG. 4. As in Fig. 3, but both Ku- and Ka-band reflectivity observations are used in the estimation.

significant improvement when estimates are derived from triple-frequency observations. This is rather a statistical artifact that is due to the fact that there are no sampling errors in the estimation process, the inversion and the evaluation PSDs being drawn from the same distribution. To test the robustness of the nonparametric approach, we perturb the computed reflectivity with random noise with mean 0.0 and standard deviation 3.0 dB and repeat the calculations shown in Fig. 5 and described in the bottom row of Table 1. Results indicate

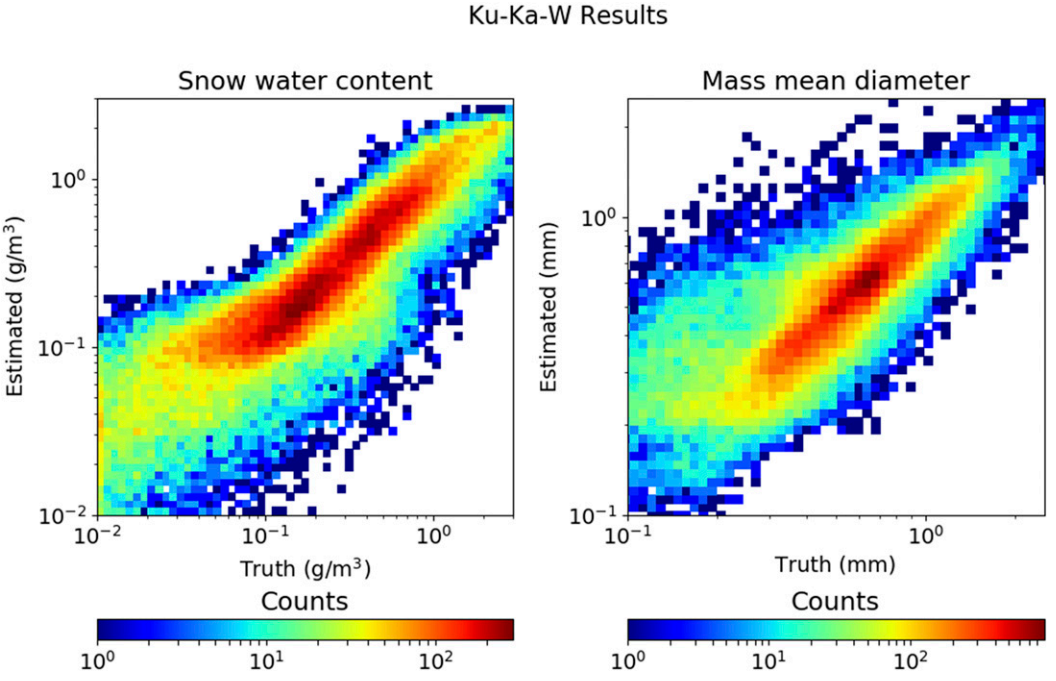

FIG. 5. As in Fig. 3, but triple-frequency reflectivity observations are used in the estimation.

TABLE 1. Statistical scores quantifying the agreement between estimates and the true values. Scores include the coefficient of correlation, normalized root-mean-square error, and normalized mean error. Results are derived by drawing the a priori and the validation subsets from the OLYMPEX dataset.

	IWC			D_m		
Obs	CC	NRMSE (%)	NME (%)	CC	NRMSE (%)	NME (%)
Ku	0.80	60.07	0.16	0.84	53.78	0.11
Ku, Ka	0.81	58.43	−0.73	0.84	54.40	0.31
Ku, Ka, W	0.87	49.20	−1.16	0.87	49.75	0.10

an increase in the NRMSE by about 30% for both the IWC and D_m. Similarly, the correlation coefficients decreases by about 8%for both variables, but the bias is still negligible for both variables.

In real applications, however, it is expected that single-frequency estimates will not be as accurate as the results in Fig. 3 suggest. This is because the distribution of PSD parameters is known to vary significantly both seasonally and geographically (Delanoe et al. 2005, 2014) and automatically determining the most appropriate distributions of PSDs in the inversion database may be difficult. Shown in Fig. 6 are CFADs of the logarithm of the scale factor and of the mass mean diameter derived using all PSD data collected during IPHEX. As is apparent in Fig. 6, and consistent with the findings of Delanoe et al. (2005, 2014), there are significant differences in the vertical distribution of N_w and D_m relative to the OLYMPEX distributions. It is, therefore, expected that application of the estimation method driven by OLYMPEX inversion information to IPHEX-calculated reflectivity observations will result in poorer performance. The three statistical scores (CC, NRMSE, and NME) of such an evaluation are reported in Table 2. Relative to the results in Table 1, poorer performance (i.e., lower correlations, larger random errors, and even significant biases) is apparent in Table 2. However, the performance is satisfactory for the triple-frequency estimates. The distributions of estimates as a function the true values are shown in Fig. 7. It may be seen in Fig. 7 that while the estimates are

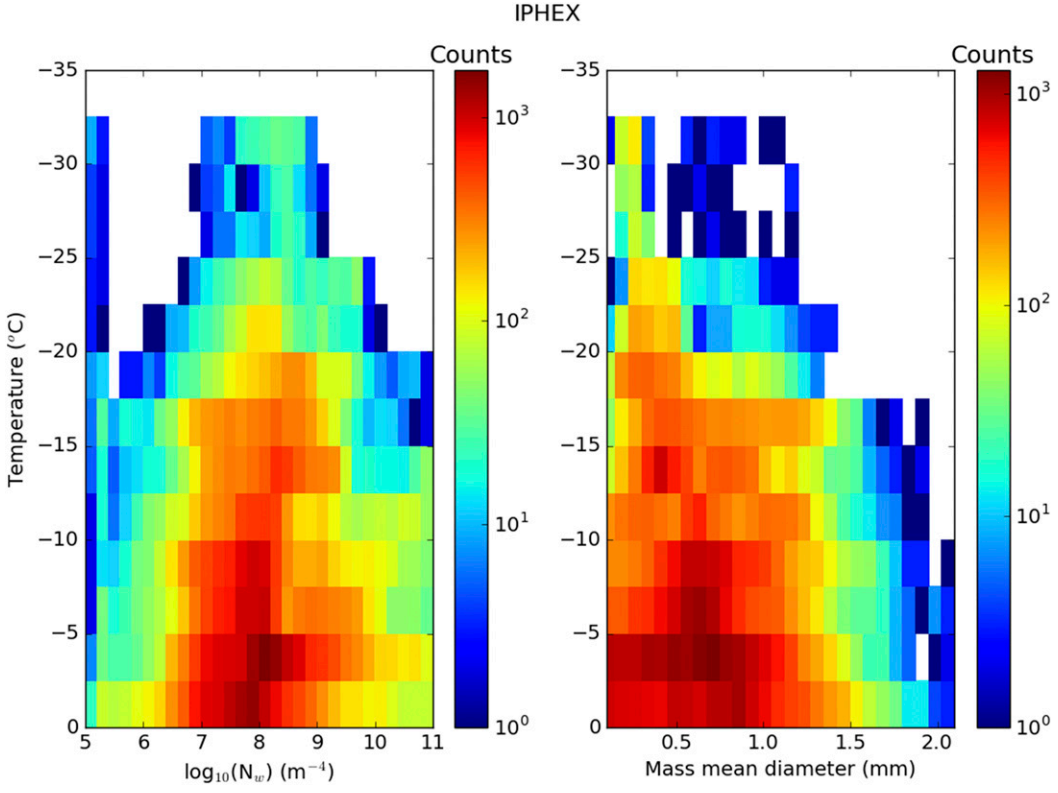

FIG. 6. As in Fig. 2, but for IPHEX observations.

TABLE 2. As in Table 1, but drawing the a priori information from the OLYMPEX dataset and the validation data from the IPHEX dataset.

	IWC			D_m		
Obs	CC	NRMSE (%)	NME (%)	CC	NRMSE (%)	NME (%)
Ku	0.67	78.77	30.236	0.75	68.74	−11.20
Ku, Ka	0.72	72.89	29.436	0.76	68.35	−13.130
Ku, Ka, W	0.85	53.96	14.033	0.83	58.26	−10.133

strongly correlated with the true variables, they are also biased, especially at the low end of the distribution. This is because the DWR signature of small particles may be dominated by noise and not have a significant impact on the estimates. In these conditions, estimates are likely to be affected more by the climatology of PSDs in the inversion database than by the DWR values. Since ice particles during OLYMPEX tended to be generally smaller than in IPHEX, IPHEX estimates with OLYMPEX a priori information are characterized by underestimation of the mass mean diameter and overestimation of the ice water content. Nevertheless, biases are significantly smaller when all three frequencies are used.

The impact of uncertainties in the scattering properties may be simply investigated by assuming a certain type of particle in the generation of the inversion PSD reflectivity database and a potentially different type of particles in the generation of the evaluation database. Since the scattering properties of three types of particles (see Fig. 1) are readily available, nine combinations of inversion–evaluation databases can be investigated. The biases associated with uncertainties in the particle types are given in Table 3. Every entry in the table (which is derived exclusively using OLYMPEX PSDs) is associated with a particle type in the calculation of the reflectivity observations used in the evaluation and a potentially different particle type assumed in the generation of the inversion PSD-reflectivity database. For example, the estimated bias associated with Lu et al. (2016) graupel particles, when assuming that they are Liu (2008) aggregates (ScatDB), is specified in the third position of the first row of Table 3 (i.e., 10.41%). From the results in Table 3, it may be concluded that estimates that are based on ScatDB (Liu 2008) a priori information work satisfactorily for both denser and less dense

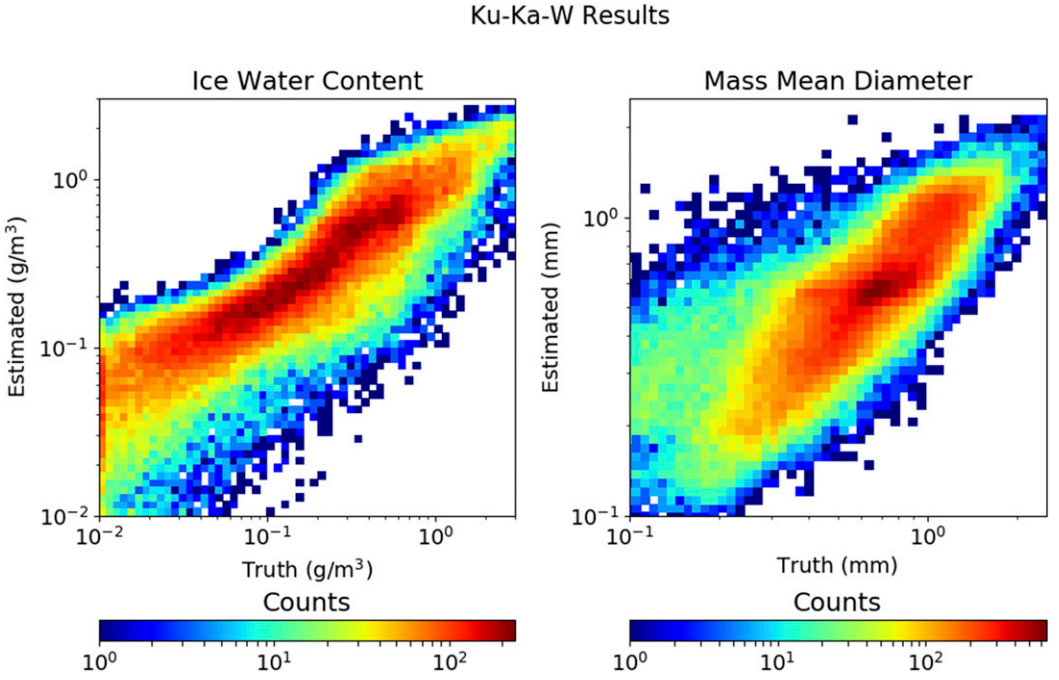

FIG. 7. As in Fig. 5, but for observations computed from IPHEX PSDs and using OLYMPEX PSDs in the estimation process.

TABLE 3. Relative biases (NME) caused by the use of different particle types in the triple-frequency estimates. For any given row, the same particle type is used in the generation of the a priori information; for a given column, the same particle type is used in the generation of the evaluation reflectivity.

		Actual particle type		
		ScatDB	PSU aggregates	PSU graupel
Assumed particle type	ScatDB	−0.41%	−12.47%	10.41%
	PSU aggregates	21.85%	−0.22%	33.81%
	PSU graupel	−7.10%	−16.04%	−0.48%

particles [i.e., Lu et al. (2016) graupel and Lu et al. (2016) aggregates].

To investigate the performance of the particle-type classification procedure described in the previous section, we calculate the reflectivity associated with the OLYMPEX PSDs for all the three types of particles in Fig. 1 and include them in the same PSD–reflectivity database. The database is randomly split into two subsets. One subset is used to provide the inversion relationships, and the other is for validation. The confusion matrix of the classification procedure is reported in Table 4. That is, the distribution of predicted particle types as a function of their true type is given in the three columns of a given row. If the classification were perfect, the elements on the top-down and left–right diagonal would be 100%. As is apparent in Table 4, the ScatDB (Liu 2008) particles are the most difficult to classify correctly. At the same type, these are the particles associated with the smallest biases (see Table 3) when incorrectly used. An interpretation of the results in Table 3 might be that the classification of ice particles on the basis of triple-frequency radar observations is more difficult and less accurate than has been suggested in previous studies (e.g., Kneifel et al. 2011). However, the results here should be interpreted as a lower bound, because the magnitude of the noise added to the observations is significant. Also, the three types of particles considered in this study, although realistic, do not capture the entire spectrum of particle shapes and their associated scattering properties. Furthermore, different types of particles may occur within the same PSD.

Another source of uncertainty in the estimates is the liquid cloud water. Liquid cloud water may significantly attenuate the observations at Ka and W bands and needs to be accounted for in the estimation procedure. The challenge in accounting for cloud water attenuation in the estimates stems from the fact cloud water is strongly connected to a large variety of synoptic, mesoscale, and microphysical processes and can occur as high as 3–4 km above the freezing level (Matejka et al. 1980). This makes the development of reliable parameterizations difficult. The analysis of in situ observations from OLYMPEX and IPHEX shows that 70% of nonzero ice water content observations are below $0.1\,\mathrm{g\,m^{-3}}$. We, therefore, investigate the sensitivity of the IWC estimates with respect to a 1.0-km-deep layer of cloud water of magnitude $0.1\,\mathrm{g\,m^{-3}}$. That is, we just subtract the attenuation due to 1.0 km of $0.1\,\mathrm{g\,m^{-3}}$ of cloud water from the triple-frequency reflectivity observations and perform the estimation. Results show an underestimation of 7.0%. In a similar way, an overcorrection of cloud water attenuation results in a positive bias of 4.0% per $0.1\,\mathrm{g\,m^{-3}\,km^{-1}}$.

4. Application to IPHEX and OLYMPEX observations

The observations used in evaluating the method formulated in this study were collected during IPHEX (Barros et al. 2014) and the joint Olympic Mountains Experiment and Radar Definition Experiment for Aerosol–Cloud–Ecosystem (ACE) field campaign (OLYMPEX/RADEX; Houze et al. 2017). The evaluation and refinement of the current satellite precipitation estimation algorithms for the Global Precipitation Measurement Mission (GPM; Skofronick-Jackson et al. 2017), as well as the development of new algorithms for future satellite missions

TABLE 4. Confusion table showing the percentual distribution of particle classification types as a function of their actual type. Similar to Table 3, all of the particles in the same row have the same type, and columns indicate their estimated type.

		Particle classification		
		ScatDB	PSU aggregates	PSU graupel
Actual particles	ScatDB	39.55%	29.49%	30.95%
	PSU aggregates	20.02%	70.19%	9.78%
	PSU graupel	26.01%	15.62%	58.36%

such the ACE mission (Starr et al. 2010), were the primary objectives of both of these field campaigns. The focus in IPHEX was on warm-season orographic precipitation systems, whereas in OLYMPEX the focus was on extratropical cyclones and their interaction with the Olympic Mountains. The precipitation occurring in extratropical cyclones interacting with orography is the consequence of complex microphysical and mesoscale dynamic processes. Although these processes have been systematically investigated for decades (e.g., Matejka et al. 1980; Browning 2003), their quantification from spaceborne radar observations is not trivial (Houze et al. 2017). The use of multiple-frequency radar and/or coincident radiometer observations is expected to facilitate the derivation of more accurate and microphysically more insightful precipitation estimates than those typically derived from single-frequency radar observations. However, only systematic analyses based on coordinated ground and airborne observations such as those collected during OLYMPEX can objectively reveal the strengths and limitations of multiple-frequency spaceborne (or airborne) observations.

The triple-frequency (Ku, Ka, and W bands) radar observations used to investigate the method described in the previous section were collected by the NASA High-Altitude Imaging Wind and Rain Airborne Profiler (HIWRAP; Li et al. 2016) and the Cloud Radar System (CRS; Li et al. 2004) on board the NASA Earth Research-2 (ER-2; Navarro 2007) aircraft during IPHEX and OLYMPEX. The technical specifications of HIWRAP and CRS are given in Houze et al. (2017). The radar observations are collocated, but not beam matched. Given that they are two-dimensional (nadir only), we do not convolve the W- and Ka-band observations to the Ku-band radar resolution and treat differences due to observation volume mismatches as random noise. The range resolution of the three radars is the same (i.e., 37.41 m), but to speed up the processing without sacrificing accuracy we sort the initial observations into 74.82-m-resolution bins. The radars sensitivities are −8 dBZ for the Ku and Ka bands and −15 dBZ for W band at 10.0-km range. We apply a threshold to the observations at −5 dBZ for all radars and do not derive estimates unless all observations are above −5 dBZ.

Houze et al. (2017) provide brief descriptions of the synoptic context for all airborne radar measurements in OLYMPEX. In this study, we exclusively consider cases for which good coincident in situ microphysics observations exist. During both IPHEX and OLYMPEX, the 2D-S (Lawson et al. 2006) and HVPS-3 instruments were mounted on the UND Cessna Citation airplane (Heymsfield et al. 2018). These instruments collected microphysical observations during flights coordinated

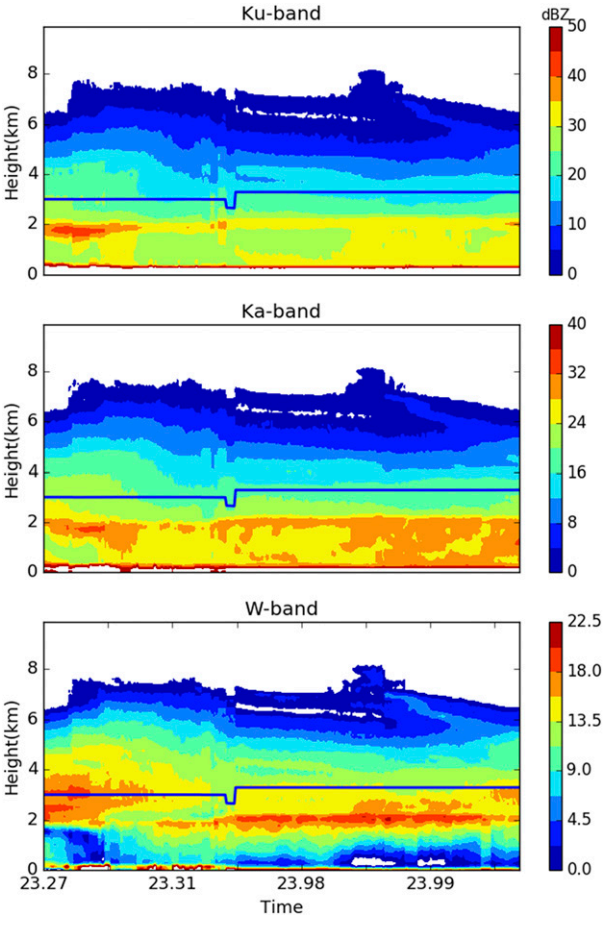

FIG. 8. Triple-frequency reflectivity observations collected by the HIWRAP/CRS during OLYMPEX on 1 Dec 2015. The blue lines indicate the altitude of the Citation airplane. The bright band apparent in the Ku- and Ka-band reflectivity observations suggests a freezing-level height of approximately 2.0 km.

with those by the NASA ER-2 aircraft. To identify radar reflectivity observations coincident with microphysical observations by instruments on board the UND Citation airplane, we loop through all the radar profiles and for each profile determine the closest UND Citation location within 6 min of the profile observation. If the distance between the profile location on the ground (defined by latitude and longitude) and of the citation aircraft is less than 0.1 km, then the radar observations are considered coincident with the in situ microphysics observations. Using this procedure, we find two OLYMPEX cases and one IPHEX case that are characterized by good coincidence between the radar and in situ observations. The OLYMPEX cases are investigated first because they provide a larger dataset of coincident observations.

Shown in Fig. 8 are the collocated Ku-, Ka-, and W-band reflectivity observations collected by HIWRAP/CRS on 1 December 2015. Note that the observations in

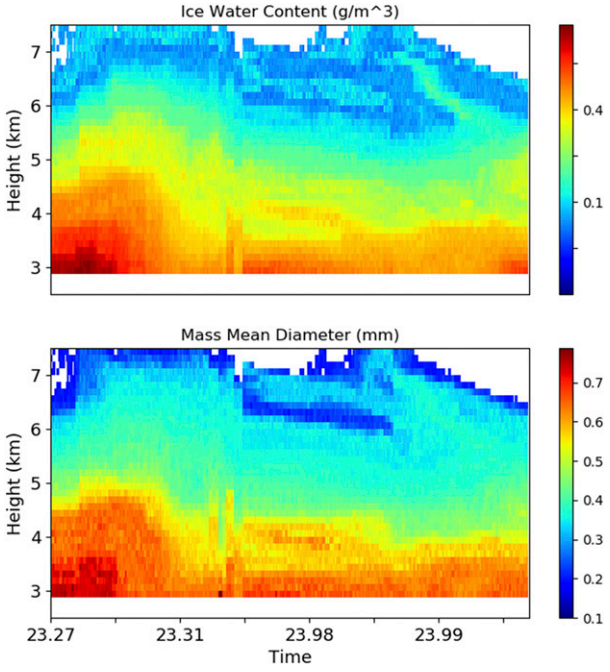

FIG. 9. (top) IWC and (bottom) D_m above the bright band derived from the triple-frequency radar observations shown in Fig. 8.

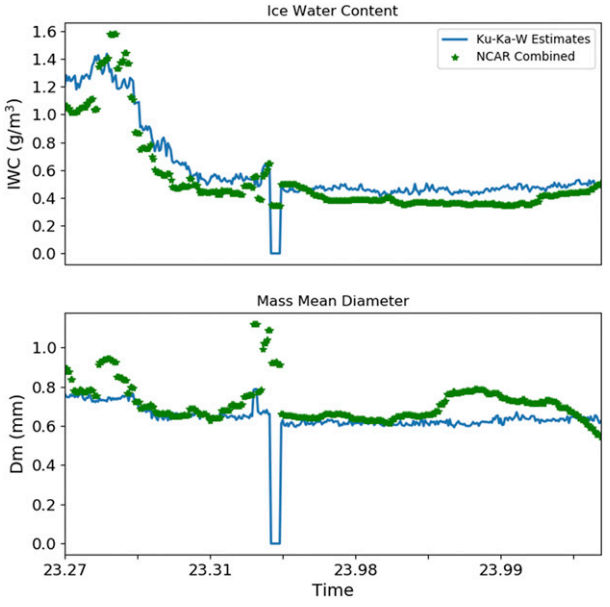

FIG. 10. (top) IWC derived from the triple-frequency radar observations and estimated from the 2D-S and HVPS instruments on board the Citation airplane using the method of Heymsfield et al. (2010) and (bottom) D_m from the radar observations and the Citation instruments.

Fig. 8 are not exclusively associated with frozen precipitation. Brightband-like structures are apparent in both the Ku- and Ka-band observations. These structures are used to identify the ice phase in a procedure similar to the GPM single-frequency precipitation classification algorithm (Awaka et al. 2016). Precipitation estimates are limited to the ice phase. Over the period shown in Fig. 8, ER-2 maintained a straight-line course multiple times with changes of directions intended to provide repeated observations over a broad stratiform region associated with a weak frontal passage. The UND Citation carried out more complex maneuvers intended to maximize the coincidence with the ER-2 observations while flying at significantly lower speeds. The reflectivity observations that could not be collocated with in situ observations using the procedure described above are not shown in Fig. 8. Consequently, there are discontinuities in the time axis. The blue line in the height–time reflectivity maps shows the altitude of the Citation. The reflectivity structures at all frequencies are indicative of stratiform precipitation. The attenuation due to water vapor is quantified from 6-hourly analyses provided by the Global Forecast System (GFS) model (Kanamitsu et al. 1991). As previously mentioned, the attenuation due to cloud water may be a significant source of uncertainty. For the three cases investigated in this paper we assume, as described in section 3, a 1.0-km-deep layer of cloud water of magnitude 0.1 g m^{-3}. The attenuation due to ice particles is handled through a gate-by-gate correction. The IWC and D_m estimated from the observations in Fig. 8 are shown in Fig. 9. As expected, the estimated IWC and D_m tend to be correlated with the observed reflectivity and to increase with temperature. However, some, most likely artifacts, are apparent in the IWC at the top of the cloud. For example, IWC estimates above 7.0 km in the 23.29–23.31 time interval tend to be larger than estimates for altitudes between 6.5 and 7.0 km for the same interval. This is most likely a consequence of noise in the observed reflectivities and of the radar systems not being beam matched. This makes the dual-wavelength ratios (which are small at the top of the cloud) hard to interpret unambiguously. Nevertheless, these artifacts are minor, and direct comparisons with in situ observations (see Fig. 10) show very good agreement.

Shown in Fig. 11 are the collocated Ku-, Ka-, and W-band reflectivity observations collected by HIWRAP/CRS on 3 December 2015. The reflectivity structures shown in Fig. 11 are more complex than those shown in Fig. 8. In particular, a band of enhanced reflectivity just above 4.0 km is apparent (most apparent in the W-band observations) between 15.35 and 15.37. While the physical processes responsible for the rapid vertical variations in the reflectivity at W band may not be reliably diagnosed from reflectivity-only observations, these variations may be the result of size sorting (Kumjian and Ryzhkov 2012) and, possibly, production of secondary ice particles (Field et al. 2017). That is, secondary ice splinters may form as

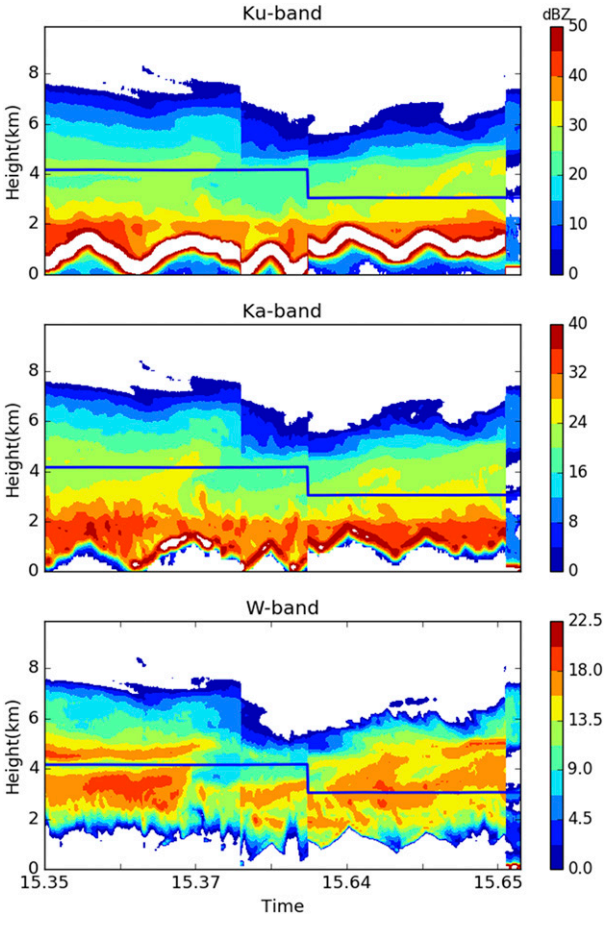

FIG. 11. As in Fig. 8, but for the 3 Dec 2015 case. The structures of the Ku- and Ka-band reflectivity observations suggest a freezing level of approximately 2.0 km (consistent with the GFS analysis product).

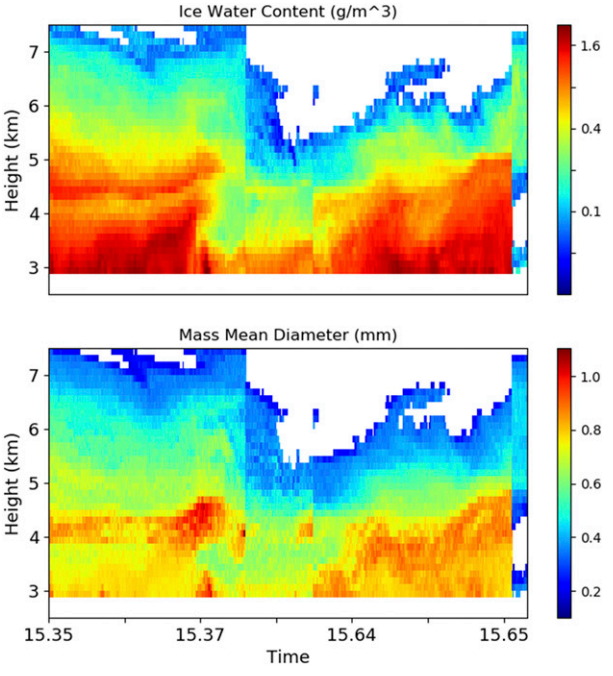

FIG. 12. As in Fig. 9, but for the 3 Dec 2015 case.

the result of water droplets shattering during freezing or of the collisional fragmentation of dendritic crystals (Bower et al. 1996; Field et al. 2017). The estimated ice water content and associated mass mean diameter are shown in Fig. 12. Consistent with the secondary-ice-production hypothesis, the estimated mass mean diameter shows strong vertical variations. Specifically, a region of smaller D_m values (i.e., $D_m \approx 0.6$ mm) associated with enhanced ice water contents at and above 4.0 km in the time interval 15.35–15.37 is noticeable in Fig. 12. The estimated IWC and associated D_m coincident with in situ observations are shown in Fig. 13. Although there is reasonable agreement between the radar and the in situ IWC estimates, there are also significant discrepancies. In particular, the radar IWC estimates in an interval straddling 15.64 are significantly smaller than the in situ estimates and the radar mass mean diameter estimates exhibit less variability than the in situ estimates. It is worth mentioning though that the in situ IWC and D_m estimates are not uncertainty free. An optimistic estimate of uncertainties in the in situ IWC estimates is 25% (Heymsfield et al. 2002). At the same time, the radar and in situ estimates are not perfectly coincident in time and space, and a time difference of a few minutes could result in significant differences between estimates.

An additional perspective on the performance of the nonparameterized triple-frequency ice estimation method can be derived through its application to radar observations collected during IPHEX. In situ microphysical observations coincident with the radar observations were more difficult to collect, because the characteristics of the precipitation systems in IPHEX were significantly different from those in OLYMPEX. Specifically, precipitation systems in IPHEX were locally more intense and shorter lived than in OLYMPEX. They were not characterized by large areas of stratiform precipitation favorable for long coordinated ER-2 and Citation flights. As a consequence, the subset of triple-frequency radar observations for which coincident in situ observations exist is much smaller than that for OLYMPEX. Shown in Fig. 14 are the triple-reflectivity observations of a stratiform rain cell on 12 June 2014. As is apparent from Fig. 14, the precipitation distribution above the bright band does not extend vertically as much as it does in the OLYMPEX cases. It also exhibits strong horizontal variability over short distances (the distance associated with the time axis in Fig. 14 is about 20 km). The radar IWC and D_m estimates and the associated in situ

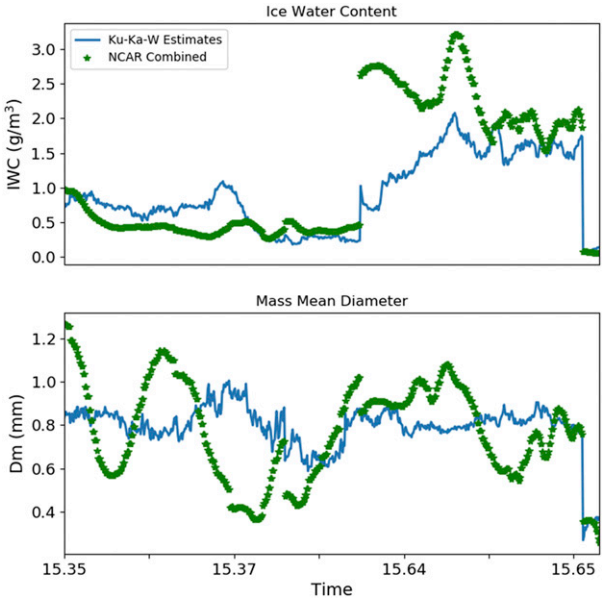

FIG. 13. As in Fig. 10, but for the 3 Dec 2015 case.

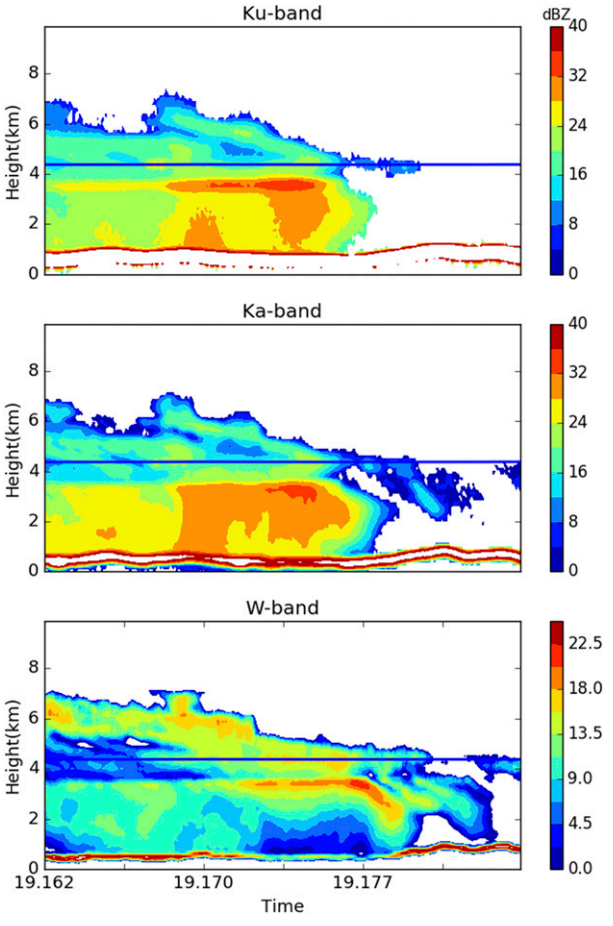

FIG. 14. Dual-frequency reflectivity observations collected by the HiWRAP/CRS during IPHEX on 12 Jun 2014. The blue lines indicate the altitude of the Citation airplane.

estimates are shown as a function of time in Fig. 15. Similar to Figs. 10 and 13, the radar and in situ IWC estimates appear to be more strongly correlated than the radar and in situ D_m estimates. The reason for this is unclear, because the cross-validation analysis (e.g., Fig. 5) suggests that estimated IWC and D_m should exhibit similar uncertainties. A plausible hypothesis is that D_m has a more complex distribution (potentially bimodal) than does IWC, which makes the estimates more sensitive to sampling errors in the a priori database.

5. Conclusions

In this study, a nonparameteric method (nPEnKS) to estimate the ice water content and the associated mass mean diameter from airborne triple-frequency observations (Ku, Ka, and W bands) is formulated and investigated. The method relies on an efficient search procedure that identifies records in a PSD reflectivity database that are characterized by reflectivity triplets within a small range from the actual observations. These records are input to an EnKS procedure to derive ice water content and mass mean diameter estimates.

The estimation method is first investigated through a cross-validation approach. In specific terms, the PSD reflectivity database is randomly separated into two disjoint subsets, and one subset is used to provide the inversion information needed by the estimation method while the other is used for validation. The cross-validation approach reveals the benefits of triple-frequency observations relative to dual- and single-frequency observations. Uncertainties and systematic errors induced by uncertainties in the a priori PSD distributions and the type of ice particles are also investigated using the cross-validation approach. In a similar way, results reveal the benefits of triple-frequency observations even though the type of ice particle does not appear to be reliably identifiable, as suggested by previous investigations.

The application of nPEnKS to real observations collected during the OLYMPEX and IPHEX field campaigns and the comparison of the derived IWC and D_m estimates with in situ estimates from cloud probes suggest performance that is generally consistent with the cross-validation analysis. To be specific, the correlations between the radar and in situ IWC estimates appear to be in the same range as those in the cross-validation analysis (i.e., 0.7–0.8). However, the agreement between radar and in situ estimates of D_m appears to be worse (significantly worse in one case) than those in the cross-validation analysis. This could be a consequence of the

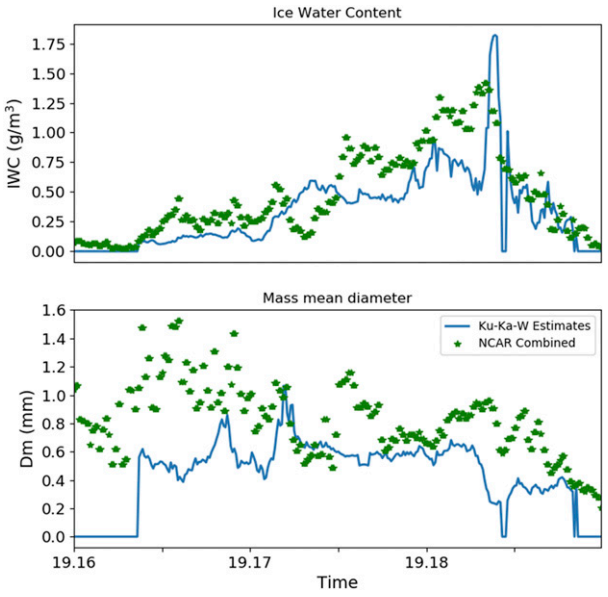

FIG. 15. As in Fig. 10, but for the 12 Jun 2014 IPHEX case.

fact that there is a potential time difference between the two types of estimates of up to 6 min, and in an Eulerian framework PSDs may change significantly in a 6-min interval. At the same time, especially given complex processes such as ice splintering and aggregation, it is possible that the ice particles and the associated backscattering properties considered in this study do not cover the entire spectrum encountered in nature, which may occasionally result in significantly larger errors than expected from the statistics of the cross-validation studies.

The extension of nPEnKS to satellite applications using a sequential-processing strategy is straightforward. That is, the method can be structured in two distinct steps. In the first step, nPEnKS can be applied, as is, to derive ensembles of IWC and associated scattering estimates at W band from downscaled Ku- and Ka-band observations (Grecu et al. 2016). In the second, the ensembles of IWC and scattering properties can be used to simulate W-band observations using a fast multiple-scattering radar model (Hogan and Battaglia 2008) and to derive final estimates using the ensemble Kalman filter smoother.

Acknowledgments. This work was supported by the NASA Remote Sensing Theory project through Grant NNX15AQ21G. The authors thank Dr. Lucia Tsaoussi (NASA Headquarters) for her support of this effort. Funding from NASA to NCAR on Grant NNX16AQ52G and from the Japanese Space Agency (JAXA) is greatly appreciated. The authors also thank Drs. Mei Han and Scott Braun for providing cloud-resolving simulations used in evaluating some of the numerical tools used in this paper and two anonymous reviewers for their insightful comments.

REFERENCES

Agarwal, P. K., and J. Erickson, 1999: Geometric range searching and its relatives. *Advances in Discrete and Computational Geometry*, B. Chozelle, J. E. Goodman, and R. Pollock, Eds., Contemporary Mathematics, Vol. 223, American Mathematical Society, 1–56, https://doi.org/10.1090/conm/223/03131.

Anderson, J. L., 2003: A local least squares framework for ensemble filtering. *Mon. Wea. Rev.*, **131**, 634–642, https://doi.org/10.1175/1520-0493(2003)131<0634:ALLSFF>2.0.CO;2.

Awaka, J., M. Le, V. Chandrasekar, N. Yoshida, T. Higashiuwatoko, T. Kubota, and T. Iguchi, 2016: Rain type classification algorithm module for GPM dual-frequency precipitation radar. *J. Atmos. Oceanic Technol.*, **33**, 1887–1898, https://doi.org/10.1175/JTECH-D-16-0016.1.

Barros, A., and Coauthors, 2014: NASA GPM-ground validation: Integrated Precipitation and Hydrology Experiment 2014 science plan. NASA Doc., 64 pp., https://doi.org/10.7924/G8CC0XMR.

Battaglia, A., K. Mroz, T. Lang, F. Tridon, S. Tanelli, L. Tian, and G. M. Heymsfield, 2016: Using a multiwavelength suite of microwave instruments to investigate the microphysical structure of deep convective cores. *J. Geophys. Res. Atmos.*, **121**, 9356–9381, https://doi.org/10.1002/2016JD025269.

Bower, K. N., S. J. Moss, D. W. Johnson, T. W. Choularton, J. Latham, P. R. A. Brown, A. M. Blyth, and J. Cardwell, 1996: A parametrization of the ice water content observed in frontal and convective clouds. *Quart. J. Roy. Meteor. Soc.*, **122**, 1815–1844, https://doi.org/10.1002/qj.49712253605.

Browning, K. A., 2003: Mesoscale substructure of extratropical cyclones observed by radar. *Radar and Atmospheric Science: A Collection of Essays in Honor of David Atlas*, *Meteor. Monogr.*, No. 52, Amer. Meteor. Soc., 7–32, https://journals.ametsoc.org/toc/amsm/52.

Delanoë, J., and R. J. Hogan, 2008: A variational scheme for retrieving ice cloud properties from combined radar, lidar, and infrared radiometer. *J. Geophys. Res.*, **113**, D07204, https://doi.org/10.1029/2007JD009000.

——, A. Protat, J. Testud, D. Bouniol, A. J. Heymsfield, A. Bansemer, P. R. A. Brown, and R. M. Forbes, 2005: Statistical properties of the normalized ice particle size distribution. *J. Geophys. Res.*, **110**, D10201, https://doi.org/10.1029/2004JD005405.

——, A. J. Heymsfield, A. Protat, A. Bansemer, and R. J. Hogan, 2014: Normalized particle size distribution for remote sensing application. *J. Geophys. Res. Atmos.*, **119**, 4204–4227, https://doi.org/10.1002/2013JD020700.

Evensen, G., 2006: *Data Assimilation: The Ensemble Kalman Filter*. Springer-Verlag, 280 pp.

Field, P. R., and Coauthors, 2017: Secondary ice production: Current state of the science and recommendations for the future. *Ice Formation and Evolution in Clouds and Precipitation: Measurement and Modeling Challenges*, *Meteor. Monogr.*, No. 58, Amer. Meteor. Soc., 7.1–7.20, https://journals.ametsoc.org/doi/pdf/10.1175/AMSMONOGRAPHS-D-16-0014.1.

Gong, J., and D. L. Wu, 2017: Microphysical properties of frozen particles inferred from Global Precipitation Measurement (GPM) Microwave Imager (GMI) polarimetric measurements. *Atmos. Chem. Phys.*, **17**, 2741–2757, https://doi.org/10.5194/acp-17-2741-2017.

Grecu, M., L. Tian, W. S. Olson, and S. Tanelli, 2011: A robust dual-frequency radar profiling algorithm. *J. Appl. Meteor.*, **50**, 1543–1557, https://doi.org/10.1175/2011JAMC2655.1.

——, W. S. Olson, S. J. Munchak, S. Ringerud, L. Liao, Z. Haddad, B. L. Kelley, and S. F. McLaughlin, 2016: The GPM combined algorithm. *J. Atmos. Oceanic Technol.*, **33**, 2225–2245, https://doi.org/10.1175/JTECH-D-16-0019.1.

Hastie, T., R. Tibshirani, and J. Friedman, 2009: *The Elements of Statistical Learning Data Mining, Inference, and Prediction*. 2nd ed. Springer, 745 pp., http://www-stat.stanford.edu/~tibs/ElemStatLearn/.

Heymsfield, A. J., A. Bansemer, P. R. Field, S. L. Durden, J. L. Stith, J. E. Dye, W. Hall, and C. A. Grainger, 2002: Observations and parameterizations of particle size distributions in deep tropical cirrus and stratiform precipitating clouds: Results from in situ observations in TRMM field campaigns. *J. Atmos. Sci.*, **59**, 3457–3491, https://doi.org/10.1175/1520-0469(2002)059<3457:OAPOPS>2.0.CO;2.

——, ——, C. Schmitt, C. Twohy, and M. R. Poellot, 2004: Effective ice particle densities derived from aircraft data. *J. Atmos. Sci.*, **61**, 982–1003, https://doi.org/10.1175/1520-0469(2004)061<0982:EIPDDF>2.0.CO;2.

——, C. Schmitt, A. Bansemer, and C. H. Twohy, 2010: Improved representation of ice particle masses based on observations in natural clouds. *J. Atmos. Sci.*, **67**, 3303–3318, https://doi.org/10.1175/2010JAS3507.1.

——, A. Bansemer, N. B. Wood, G. Liu, S. Tanelli, O. O. Sy, M. Poellot, and C. Liu, 2018: Toward improving ice water content and snow-rate retrievals from radars. Part II: Results from three wavelength radar–collocated in situ measurements and *CloudSat*–GPM–TRMM radar data. *J. Appl. Meteor. Climatol.*, **57**, 365–389, https://doi.org/10.1175/JAMC-D-17-0164.1

Hogan, R. J., and A. Battaglia, 2008: Fast lidar and radar multiple-scattering models. Part II: Wide-angle scattering using the time-dependent two-stream approximation. *J. Atmos. Sci.*, **65**, 3636–3651, https://doi.org/10.1175/2008JAS2643.1.

Houze, R. A., Jr., and Coauthors, 2017: The Olympic Mountains Experiment (OLYMPEX). *Bull. Amer. Meteor. Soc.*, **98**, 2167–2188, https://doi.org/10.1175/BAMS-D-16-0182.1.

Kanamitsu, M., and Coauthors, 1991: Recent changes implemented into the Global Forecast System at NMC. *Wea. Forecasting*, **6**, 425–435, https://doi.org/10.1175/1520-0434(1991)006<0425:RCIITG>2.0.CO;2.

Kneifel, S., M. S. Kulie, and R. Bennartz, 2011: A triple-frequency approach to retrieve microphysical snowfall parameters. *J. Geophys. Res.*, **116**, D11203, https://dx.doi.org/10.1029/2010JD015430.

——, A. von Lerber, J. Tiira, D. Moisseev, P. Kollias, and J. Leinonen, 2015: Observed relations between snowfall microphysics and triple-frequency radar measurements. *J. Geophys. Res. Atmos.*, **120**, 6034–6055, https://doi.org/10.1002/2015JD023156.

Kulie, M. S., M. J. Hiley, R. Bennartz, S. Kneifel, and S. Tanelli, 2014: Triple-frequency radar reflectivity signatures of snow: Observations and comparisons with theoretical ice particle scattering models. *J. Appl. Meteor. Climatol.*, **53**, 1080–1098, https://doi.org/10.1175/JAMC-D-13-066.1.

Kumjian, M. R., and A. V. Ryzhkov, 2012: The impact of size sorting on the polarimetric radar variables. *J. Atmos. Sci.*, **69**, 2042–2060, https://doi.org/10.1175/JAS-D-11-0125.1.

Kummerow, C. D., D. L. Randel, M. Kulie, N.-Y. Wang, R. Ferraro, S. J. Munchak, and V. Petkovic, 2015: The evolution of the Goddard profiling algorithm to a fully parametric scheme. *J. Atmos. Oceanic Technol.*, **32**, 2265–2280, https://doi.org/10.1175/JTECH-D-15-0039.1.

Kuo, K.-S., and Coauthors, 2016: The microwave radiative properties of falling snow derived from nonspherical ice particle models. Part I: An extensive database of simulated pristine crystals and aggregate particles, and their scattering properties. *J. Appl. Meteor. Climatol.*, **55**, 691–708, https://doi.org/10.1175/JAMC-D-15-0130.1.

Lawson, R. P., D. O'Connor, P. Zmarzly, K. Weaver, B. Baker, Q. Mo, and H. Jonsson, 2006: The 2D-S (stereo) probe: Design and preliminary tests of a new airborne, high-speed, high-resolution particle imaging probe. *J. Atmos. Oceanic Technol.*, **23**, 1462–1477, https://doi.org/10.1175/JTECH1927.1.

Leinonen, J., and W. Szyrmer, 2015: Radar signatures of snowflake riming: A modeling study. *Earth Space Sci.*, **2**, 346–358, https://doi.org/10.1002/2015EA000102.

Li, L., G. M. Heymsfield, P. E. Racette, L. Tian, and E. Zenker, 2004: A 94-GHz cloud radar system on a NASA high-altitude ER-2 aircraft. *J. Atmos. Oceanic Technol.*, **21**, 1378–1388, https://doi.org/10.1175/1520-0426(2004)021<1378:AGCRSO>2.0.CO;2.

——, and Coauthors, 2016: The NASA High-Altitude Imaging Wind and Rain Airborne Profiler. *IEEE Trans. Geosci. Remote Sens.*, **54**, 298–310, https://doi.org/10.1109/TGRS.2015.2456501.

Liu, G., 2008: A database of microwave single-scattering properties for nonspherical ice particles. *Bull. Amer. Meteor. Soc.*, **89**, 1563–1570, https://doi.org/10.1175/2008BAMS2486.1.

Liu, T., A. W. Moore, and A. Gray, 2006: New algorithms for efficient high-dimensional nonparametric classification. *J. Mach. Learn. Res.*, **7**, 1135–1158, http://www.jmlr.org/papers/volume7/liu06a/liu06a.pdf.

Lu, Y., Z. Jiang, K. Aydin, J. Verlinde, E. E. Clothiaux, and G. Botta, 2016: A polarimetric scattering database for non-spherical ice particles at microwave wavelengths. *Atmos. Meas. Tech.*, **9**, 5119–5134, https://doi.org/10.5194/amt-9-5119-2016.

Matejka, T. J., R. A. Houze Jr., and P. V. Hobbs, 1980: Microphysics and dynamics of clouds associated with mesoscale rainbands in extratropical cyclones. *Quart. J. Roy. Meteor. Soc.*, **106**, 29–56, https://doi.org/10.1002/qj.49710644704.

Navarro, R., 2007: The NASA Earth Research-2 (ER-2) aircraft: A flying laboratory for Earth science studies. NASA Tech. Memo. NASA/TM-2007-214615, 8 pp., https://ntrs.nasa.gov/archive/nasa/casi.ntrs.nasa.gov/20070014865.pdf.

Petrie, R. E., and S. L. Dance, 2010: Ensemble-based data assimilation and the localisation problem. *Weather*, **65** (3), 65–69, https://doi.org/10.1002/wea.505.

Sekhon, R. S., and R. C. Srivastava, 1970: Snow size spectra and radar reflectivity. *J. Atmos. Sci.*, **27**, 299–307, https://doi.org/10.1175/1520-0469(1970)027<0299:SSSARR>2.0.CO;2.

Skofronick-Jackson, G., and Coauthors, 2017: The Global Precipitation Measurement (GPM) mission for science and society.

Bull. Amer. Meteor. Soc., **98**, 1679–1695, https://doi.org/10.1175/BAMS-D-15-00306.1.

Starr, D., and Coauthors, 2010: Aerosol, Cloud and Ecosystems (ACE) proposed satellite mission. NASA Study Rep., 159 pp., https://acemission.gsfc.nasa.gov/documents/Draft_ACE_Report2010%20.pdf.

Westbrook, C. D., R. C. Ball, and P. R. Field, 2006: Radar scattering by aggregate snowflakes. *Quart. J. Roy. Meteor. Soc.*, **132**, 897–914, https://doi.org/10.1256/qj.05.82.

——, ——, and ——, 2008: Corrigendum: Radar scattering by aggregate snowflakes. *Quart. J. Roy. Meteor. Soc.*, **134**, 547–548, https://doi.org/10.1002/qj.233.

Wilks, D., 2011: *Statistical Methods in the Atmospheric Sciences*. 3rd ed. Elsevier, 676 pp.

Wu, W., and G. M. McFarquhar, 2016: On the impacts of different definitions of maximum dimension for nonspherical particles recorded by 2D imaging probes. *J. Atmos. Oceanic Technol.*, **33**, 1057–1072, https://doi.org/10.1175/JTECH-D-15-0177.1.